IEEE Access
Multidisciplinary | Rapid Review | Open Access Journal

Received July 11, 2020, accepted July 20, 2020, date of publication July 27, 2020, date of current version August 6, 2020.

Digital Object Identifier 10.1109/ACCESS.2020.3012047

A Data-Driven Approach for Assembling Intertrochanteric Fractures by Axis-Position Alignment

ZIYUE DENG[1,3], JUNFENG JIANG[2,3], HONGWEI LIU[4], ZHENGMING CHENG[2,3], RUI HUANG[2,3], WENXI ZHANG[5], AND KUNJIN HE[2,3]

[1]College of Computer Science, Hohai University, Nanjing 210000, China
[2]College of IOT Engineering, Hohai University, Changzhou 213000, China
[3]Changzhou City Key Laboratory of Orthopedic Implants Digital Technology, Changzhou 213000, China
[4]Department of Orthopaedics, The Second People's Hospital of Changzhou, Changzhou 213000, China
[5]Department of Orthopaedics, The People's Hospital of Liyang, Changzhou 213000, China

Corresponding author: Junfeng Jiang (jiangjf.hhu@gmail.com)

This work was supported in part by the Natural Science Foundation of China (NSFC) under Grant 61772172 and Grant 51605142; in part by the Fundamental Research Funds for the Central Universities under Grant 2018B59814; in part by the Science and Technology Program Project Funds in Changzhou City under Grant 20195046912; in part by the Changzhou Science and Technology Support Plan Project under Grant CE20195029; in part by the Key Scientific Projects of Changzhou Public Health and Family Planning Commission under Grant ZD201510; and in part by the Jiangsu Natural Science Foundation under Grant BK20181158.

ABSTRACT In clinics, the reduction of femoral intertrochanteric fractures should meet the medical demands of both axis alignment and position alignment. State-of-the-art approaches are designed for merely position alignment, not allowing for axis alignment. The axis-position alignment can be formulated as a least square optimization problem with the inequality constraints. The main challenges include how to solve this constrained optimization problem and effectively extract the semantic of the randomly fractured bone pieces. To address these problems, a semi-automatic data-driven method is introduced. First, the medical semantic parameters are computed, at the beginning of when the 3D input pieces' anatomical areas are labeled by using the deep neural network. A statistical shape model is leveraged to generate the synthetic training data so as to learn the anatomical landmarks of the pieces, greatly reducing the labeling costs for training. The final reduction position of the pieces is obtained through iterative axis alignment and position alignment. Our method is evaluated by three baselines, i.e., the manual assembly of the orthopaedic specialists and two typical bone assembling methods. The presented method solves an optimization problem for assembling intertrochanteric fracture by axis-position alignment. All cases can be successfully assembled with the developed algorithm which is proved to be capable of reaching the clinical demand.

INDEX TERMS 3D model, intertrochanteric fracture, fracture reduction, data-driven, axis-position alignment.

I. INTRODUCTION

When a fracture occurs in the human body, the treatment usually requires the assembling and fixation of the bone fragments. The assembling of the bone fragments is called fracture reduction in clinical practice [1]. During the operation, fracture reduction usually depends on the doctor's experience, which sometimes leads to lower efficiency and more redundant radiation exposure, resulting in delayed fracture healing, fracture nonunion, infection, and other surgical complications. With the development and maturation of computer-aided design and computer graphics research, the preoperative use of computers for three-dimensional fracture reduction [2], [3] can improve the accuracy of intraoperative surgical reduction and shorten the operation time.

The state-of-the-art of fracture reduction methods [3] only consider aligning the fracture boundaries, which we call position alignment. These methods will probably fail in the scenarios that the boundaries can be impossibly matched due to missing of pieces and the cluttered/blurred boundaries.

The associate editor coordinating the review of this manuscript and approving it for publication was Liang-Bi Chen.

Pieces missing and boundaries blurring are common situations for most of the intertrochanteric fractures [4]. To handle these problems, the orthopaedic specialists will usually enforce the angles between the bone axes of the lower at least to be in a reasonable range, and the fracture boundaries as close as possible, assuring the lower limbs to be basically functional (see Fig.1). The alignment demands of maintaining the proper angles between bone axes are called axis-alignment. As a matter of fact, this kind of axis-position alignment is extensively demanded for assembling the major types of the fractures of the human limbs, which can be formulated as a constrained assembly optimization problem. To solve the axis-position alignment problem, the main technical challenge is how to effectively extract the axes of randomly fractured bones.

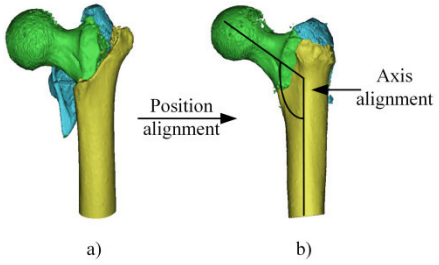

FIGURE 1. Fracture reduction of intertrochanteric fractures. a) Fracture bones. b) Reduction result.

In this study, we put up with a data-driven approach to extract the bone axes and iteratively solve the constrained assembly problem for intertrochanteric fractures. Technically, our study opens the door of the research for the new problems of constrained assembling of bone pieces in order to meet the practical demands in clinics. And, our study also paves the way for the axis-position alignment of the other kinds of bone fractures.

II. RELATED WORK

Fracture reduction involves the extraction of medical semantics of bones. Therefore, the research progress of fracture reduction and the extraction of medical semantics are separately introduced.

A. FRACTURE REDUCTION

Fracture reduction falls into the field of digital assembly for fractured pieces, as was originated from the jigsaw puzzle games [5] and was later used in archaeological restoration [6] and fracture reduction for bones [7]–[11]. Next, we will introduce the fragments reassembly methods in detail according to different classification criteria.

The objects to be reassembled can be divided into three categories, i.e., image fragments [12]–[14], archaeological fragments [15], and fractured bones [9], [16]. They differ mainly in the ways of how they are generated as the digital input. The images are known as the Euclidean data [14], comprised of regular 2D pixels. The archaeological fragments are scanned by laser-scanners to reconstruct their 3D shapes. Different from the former, the 3D shapes of bones are mostly reconstructed from the CT images. The boundaries of the 3D bones are usually blurred due to the limitation of the precision of CT scanners.

The similar shape of pieces, if available, can be used as a prior knowledge or template to guide the assembly. For example, the healthy side of the bones (we call contralateral bone) can be utilized to aid the assembly of the fractured side [7], [9]. However, [16] suggests that there exists possible shape difference between the symmetric sides of the bones. And usually, the healthy side is not available because only the fractured side will be scanned in clinics. When the templates are not available, the approaches will assemble the bone pieces by aligning the boundaries of the pieces [11]. Thus, the errors of assembly depend on the resolution and the quality of 3D reconstruction of the boundaries in great extent. As for the intertrochanteric fractures, the pieces' boundaries will always blur because of the low bone mineral density of this area. As a result, this kind of work will probably fail, not to mention maintaining the proper angle of the axes.

Fragments matching can be divided into pair-wise local matching [8], [15], [18] and multi-piece global matching [6], [9], [16], [17]. The pair-wise approaches take two pieces as one unit for assembly, conducting the assembling by matching their fractured boundaries. The assembly work for multi-pieces always takes the pair-wise assembly as the first step to create the candidates matches between the pieces. The main challenge for the multi-piece assembly is to keep the global consistancy for all the pieces, which is known as notorious NP-hard problem. The Greedy algorithm [6] and the branch-and-bound method [17] are usually utilized as the approximate numerical solutions for the optimization.

In practical operations, the assembly for intertrochanteric fractures considers only two primary bone pieces, i.e., the femoral piece and the femoral shaft piece. Thus, our goal is to assemble these two pieces to assure the axes angles to be in the normal range, meanwhile, the fracture boundaries should be as close as possible.

B. EXTRACTION OF MEDICAL SEMANTICS FROM BONES

Labeling the regions of the 3D shapes has been extensively studied in the area of computer graphics, where there are too many related work to be enumerated. In the following, we are about to introduce the work which is closely related. The approaches can be divided into the non-data-driven ones and data-driven ones, which will be discussed as follows.

In the early studies, [19]–[24] use the spatial relationships among the landmarks of the bones. Some work [25], [26] labels the landmarks by matching the target to the templates and propagating the landmarks from the template to the target. The challenge is how to match the target to the templates, which is an open problem in the field of computer graphics. Matching the pieces to the complete bone template can be formulated as the NP-hard problem of partial matching.

The convolutional neural networks (CNNs) in many fields such as computer vision, the geometrical deep learning has become the off-the-shelf approaches to handle the 3D shape analysis. Specially, to label the region of the 3D objects, numerous CNN-like networks are proposed for different tasks and have outstanding performance over the traditional non-data-driven methods. For example, Pointnet^{++} [27], taking the point cloud as input, is capable of handling the tasks from object classification to segmentation. The recent MeshCNN [28] is a convolutional neural network designed specifically for triangular meshes. MeshCNN utilizes the unique properties of the mesh for a direct analysis of 3D shapes. 3D ShapeNets [29] represents a geometric 3D shape as a probability distribution of binary variables on a 3D voxel grid, using a Convolutional Deep Belief Network. In this paper, we choose PointNet^{++} to learn the semantic regions of the bones. To lower the cost of the labeling, we use a statistical shape model [30] so as to generate the synthetic training data. The training shapes of the femurs are generated by randomly deforming the statistical shape model. The regions on the training models can be propagated from the semantic regions pre-labeled on the mean template.

III. METHOD

A. PROBLEM FORMULATION

In this paper, taking 3D bone pieces as input, we propose a data-driven method to meet both the two requirements of the axis-position alignment. The output of our method is a collection of assembled bone pieces. The by-product of our method includes the bone semantics, e.g., semantic regions, landmarks, axes, angles, which can be used as the critical references for orthopedic surgeons treating the fractures.

Before elaborating the problem formulation, some issues need to be addressed as follows.

First, the input bone pieces are comprised of three surfaces, i.e., outer surface, inner surface, and the fracture surface (see Fig.2). The outer surface is a thin, dense membrane of bones. The inner surface is composed of the soft-tissues. The ring-like fracture surface is where the bone is fractured and is used as the fracture boundary of the piece. All the semantic regions are labeled on the outer surface.

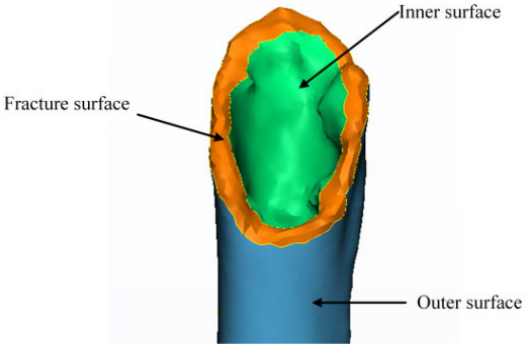

FIGURE 2. Surfaces of bone pieces.

Second, three datum planes of anthropometry are needed to be extracted, as illustrated in Fig.3. They are the axial plane, coronal plane and sagittal plane. Among them, the axial plane is parallel to the ground. The coronal and sagittal plane are perpendicular to the ground and are perpendicular to each other. The coronal plane divides the body into anterior and posterior portions, and the sagittal plane divides the body into right and left sections.

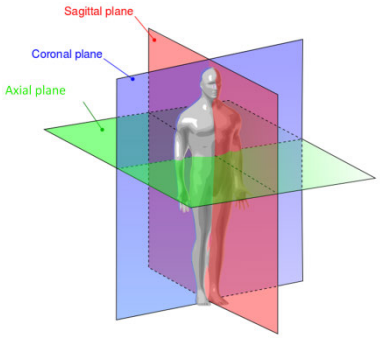

FIGURE 3. Datum planes of human body.

Third, in intertrochanteric fractures, the input fracture shapes include two primary bone pieces, namely, the piece including the femoral head (we call femoral head piece hereinafter) and the piece including the femoral shaft (we call femoral shaft piece hereinafter), as shown in Fig.4a)). During the assembly, the piece of femoral shaft is fixed, and the rigid transformation is figured for the piece of the femoral head to move from its initial position towards the femoral shaft piece (see Fig.4b)).

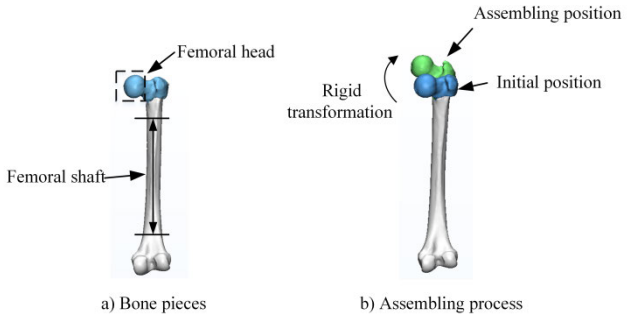

FIGURE 4. Bone pieces and assembling process.

Forth, three axes of femur are extracted including head-neck axis, shaft axis and condyle axis, as shown in Fig.5. The head-neck axis is the line connecting the center point of the femoral head and that of the femoral neck. The shaft axis is the center line of femoral shaft. And the condyle axis is the line connecting two centers of condyles of the distal femur.

Fifth, as for the intertrochanteric fracture, both two angles, i.e., the neck-shaft angle and the anteversion angle [19], need to fall into the normal ranges. The neck-shaft angle is calculated by projecting the angle between the head-neck axis and the shaft axis to the coronal plane (see Fig.6). The anteversion angle is calculated by projecting the angle between

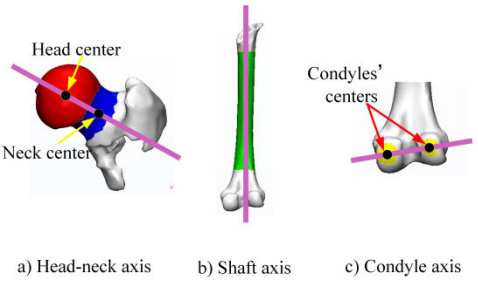

FIGURE 5. Axes of femur.

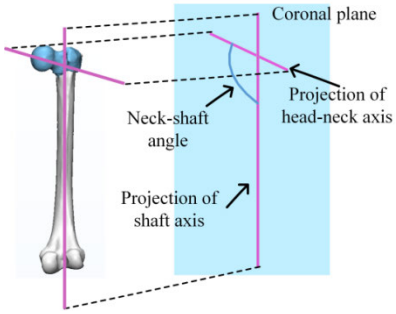

FIGURE 6. Representation of neck-shaft angle.

the head-neck axis and the condyle axis to the axial plane (see Fig.7).

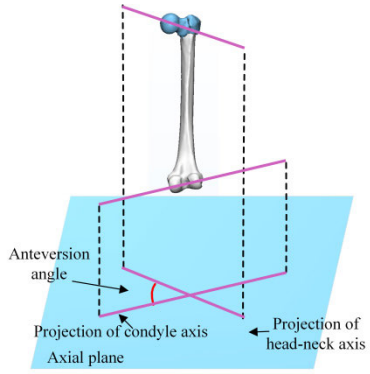

FIGURE 7. Representation of anteversion angle.

With these premises, the problem of axis-position alignment of assembling can be formulated the following least-square optimization problem with two inequality constraints.

$$\begin{cases} (R,t) = \arg\min\limits_{R,t} \sum\limits_{\substack{P_{1i}\in B_1 \\ P_{2j}\in B_2 \\ 1\le i\le n \\ 1\le j\le m}} \left\| RP_{1i} + t - P_{2j} \right\|_2^2 & (1.a) \\ \text{s.t. } \angle_c(Rl_{hn} + t, l_s) \in (\alpha_{\min}, \alpha_{\max}) & (1.b) \\ \quad \angle_a(Rl_{hn} + t, l_c) \in (\beta_{\min}, \beta_{\max}) & (1.c) \end{cases} \tag{1}$$

where (1.a) aims to minimize the average distance between the points on the two fracture surfaces (position-alignment) and (1.b) & (1.c) are the inequality constraints for axis-alignment. Specifically, R denotes the rotation matrix, t denotes the translation vector, B_1 and B_2 denote the fracture surfaces of the pieces of femoral head and femoral shaft, respectively, l_{hn} represents the head-neck axis, l_s represents the femur shaft axis, l_c represents the condyle axis, $\angle_c$ is the angle projected to the coronal plane, $\angle_a$ is the angle projected to the axial plane. Clinically, the normal ranges of the neck-shaft and anteversion angle are $[\alpha_{min}, \alpha_{max}]$ and $[\beta_{min}, \beta_{max}]$, respectively.

B. METHOD OVERVIEW

To address the optimization problem of Equation (1), we adopt an approach to conduct axis and position alignment iteratively. The overall workflow is shown in Fig. 8, which includes the following two main steps.

Step1: Extraction of the bone semantics

We use a data-driven approach to compute the bone semantics according to their hierarchical dependencies (see Fig. 9).

Step2: Axis-position alignment

The angles of the axes and the distance between the fracture pieces are alternatively adjusted until convergences.

C. DETAILS OF SEMANTICS EXTRACTION

The hierarchical dependences of the bone semantics are shown in Fig.9. Therefore, we compute the bone semantics in the order of semantic regions, landmarks, axes, datum planes, angles and distance. The details are introduced as follows.

1) EXTRACTION OF SEMANTIC REGIONS

We classify the semantic regions into two categories, i.e., the anatomical regions and the fracture surfaces. The anatomical regions include 4 regions. The anatomical regions are labeled by a data-driven method through the neural network of PointNet^{++} [27]. The fracture surfaces are extracted by the method proposed by [9]. The details are as follows.

a: EXTRACTION OF ANATOMICAL REGIONS

Firstly, the neural network is trained according to labeled point cloud data. Then, the triangle mesh models are changed into point cloud models as input data of the network. After that, the label of each point, denoting which semantic region this point belongs to, is predicted through training the network. Finally, the label of each point is mapped back to the corresponding point on the triangle mesh model. The extraction process is illustrated in Fig.10, where the head, neck, shaft and condyles are highlighted in red, blue, green, and yellow, respectively. The technical details are referred to Appendix.

b: EXTRACTION OF FRACTURE SURFACES

inspired by [9], we extract the fracture surfaces in two steps. First, we extract the initial fracture surfaces according to the

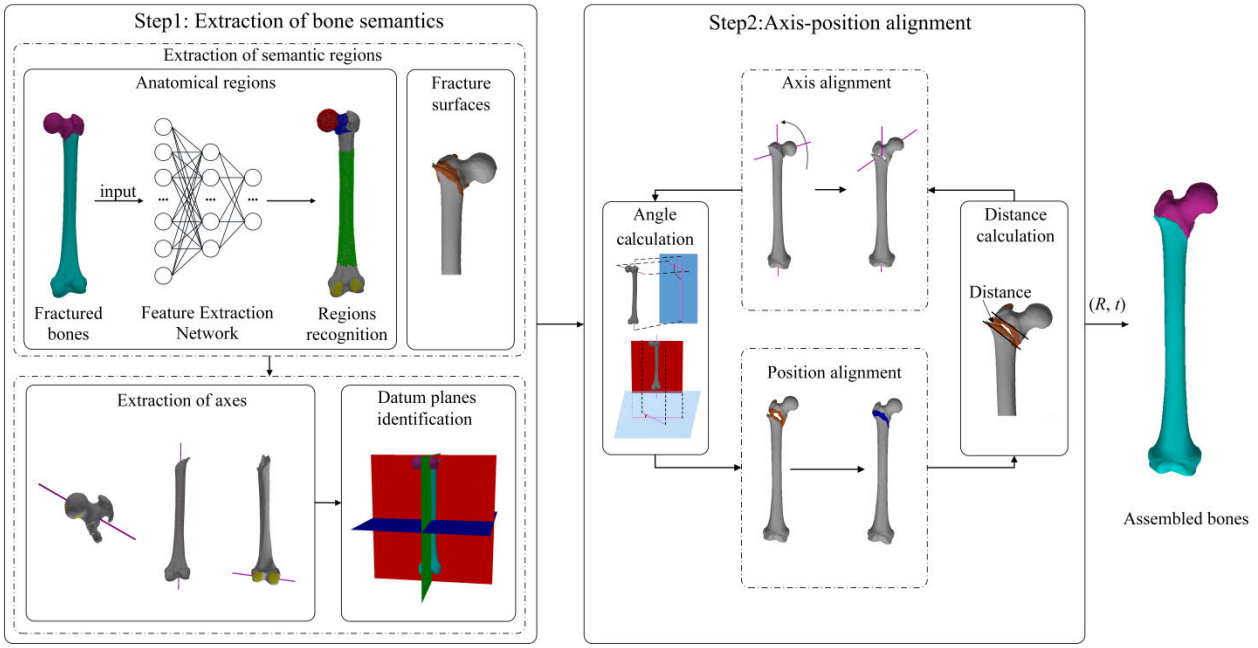

FIGURE 8. Overall workflow of our method. The method consists of two main steps, i.e., extraction of bone semantics and axis-position alignment. For extraction of bone semantics, the neural network is used to extract the semantic regions, and the axes and datum planes are identified based on the regions. The fracture surfaces are obtained based on vertex normal. For axis-position alignment, the angles of the axes and the distance between the fracture pieces are alternatively adjusted until it converges. The transform matrix (R, t) is finally calculated to assemble the fracture bones.

surface normals. Second, we refine the fracture surfaces by a post-processing. The details are as follows.

The principle of determining whether a point lying on the fracture surface by [9] are addressed in the following. Observing that the fracture surfaces of bone pieces are often narrow, [9] made two plausible assumptions. One is that the two neighboring surfaces (outer surface and inner surface) of a fracture surface are almost parallel. Another is that fracture surface is nearly perpendicular with these two neighboring surfaces. Then the normal of a point on the fracture surface is approximately perpendicular to those of the neighboring points on the outer and inner surfaces and is approximately parallel to those of the neighboring points on the same fracture surface (see Fig.11). Thus, a point can be taken as the one lying on the fracture surface if the point satisfies the above-mentioned conditions. The technical details can be referred to [9]. The thresholds of normal in our method are between $8/\pi$ and $4/\pi$.

The outliers of the fracture surface are refined by a post-processing step through region merging and trimming out the points on the anatomical regions, labeled in the previous step. The details of post-processing are as follows. Firstly, all connected regions are extracted by using a method of region growing. Secondly, the largest connected region of each fracture piece is assumed to be part of the fracture surface. Other regions of the piece, lying within a distance threshold of 0.4 mm (need to manually fine-tune according to different cases), are merged with largest region. Finally, the connected regions are updated and the process is repeated until no more regions can be added. The fracture surface of each pieces is finally identified after the fracture surface on the semantic regions are removed. One example of extracting the fracture surface of the bone pieces is illustrated in Fig. 12.

2) EXTRACTION OF AXES

The details of extracting the head-neck axis, shaft axis and condyle axis are addressed as follows.

a: HEAD-NECK AXIS

The head-neck axis is the line connecting the center point of the femoral head and that of the femoral neck. The center point of the femoral head is the sphere center, which can be fitted to the semantic region of femoral head by using the least-square method (see O_1 in Fig.13a)) [31]. The center point of the femoral neck is the centroid of the semantic region of the femoral neck (see O_2 in Fig.13a)). The details of sphere fitting are as follows.

The general equation of a sphere in x, y, and z coordinates can be seen Equation (2), the center point of the sphere with radius r is found at the point (x_0, y_0, z_0).

$$(x - x_0)^2 + (y - y_0)^2 + (z - z_0)^2 = r^2 \tag{2}$$

$$x^2 + y^2 + z^2 = 2xx_0 + 2yy_0 + 2zz_0 + r^2 - x_0^2 - y_0^2 - z_0^2 \tag{3}$$

After expanding and rearranging the terms of Equation (2), the new equation of a sphere is expressed as Equation (3). This equation can now be expressed in matrix notation as

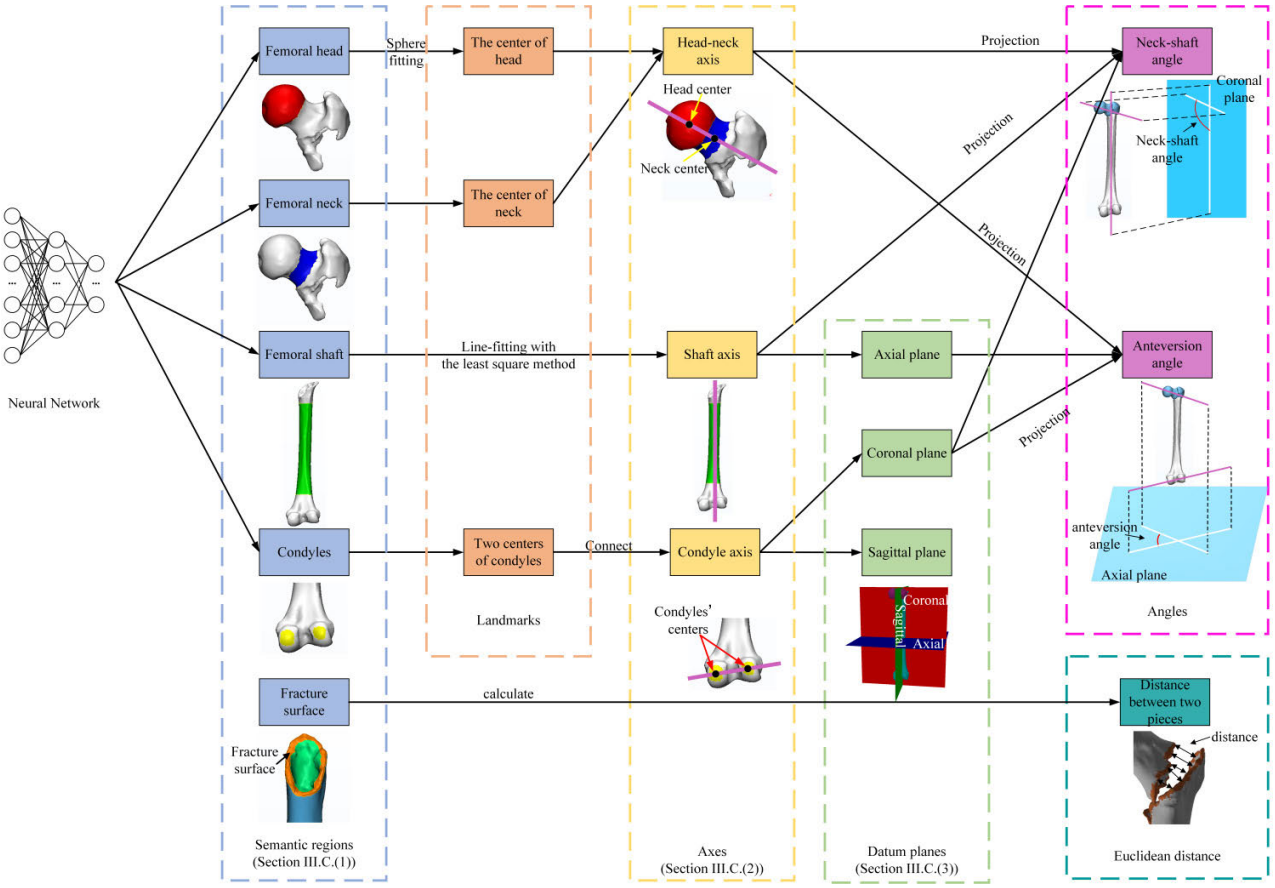

FIGURE 9. Dependence and computation of the hierarchical bone semantics. The bone semantics include five categories, which are computed in the order of semantic regions, landmarks, axes, datum planes, angles and distance. The semantic regions include anatomical regions and the fracture surfaces, the anatomical regions are labeled by using neural network. The landmarks are determined by the anatomical regions. And the axes are extracted based on the regions and landmarks. The planes can be identified through axes. Finally, angles and distance are calculated based on the above parameters.

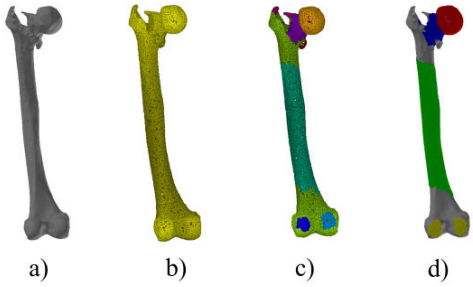

FIGURE 10. Semantic regions extraction. a) A triangle mesh model of fracture bone. b) The point cloud data obtained from the triangle mesh model. c) Predict the label of each point by deep learning. d) The label of each point is mapped to the triangle mesh model.

follow,

$$\begin{bmatrix} x_1^2+y_1^2+z_1^2 \\ x_2^2+y_2^2+z_3^2 \\ \cdots \\ x_n^2+y_n^2+z_n^2 \end{bmatrix} = \begin{bmatrix} 2x_1 & 2y_1 & 2z_1 & 1 \\ 2x_2 & 2y_2 & 2z_2 & 1 \\ \vdots & \vdots & \vdots & \vdots \\ 2x_n & 2y_n & 2z_n & 1 \end{bmatrix} * \begin{bmatrix} x_0 \\ y_0 \\ z_0 \\ r^2-x_0^2-y_0^2-z_0^2 \end{bmatrix} \tag{4}$$

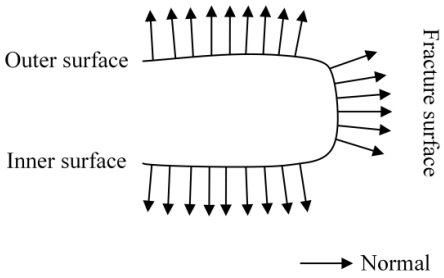

FIGURE 11. The normal of surfaces.

where x_n, y_n, z_n represent the points of head region. The sphere can be obtained by solving the Equation (4). The technical details can be referred to [31].

b: SHAFT AXIS

the femoral shaft axis is computed by fitting a line to the semantic region of femoral shaft, as illustrated in Fig.13b)).

c: CONDYLE AXIS

As shown in Fig.13c), the condyle axis is the line connecting the center points (see O_3 and O_4 in Fig.13c)) of condyle regions (yellow dots).

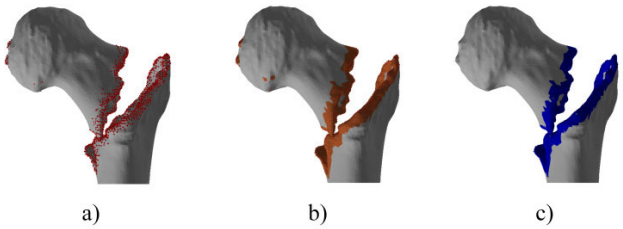

FIGURE 12. The result of fracture surface extraction. a) The sampling points of the fracture surfaces. b) The fracture surfaces of the femoral head and the femoral shaft are shown in brown. c) The fracture surface after post-processing.

3) IDENTIFICATION OF THE DATUM PLANES

The datum planes consist of the coronal, axial, and sagittal planes, which are perpendicular to each other. The three planes can be calculated based on the extracted axes. The plane perpendicular to the shaft axis is the axial plane. The coronal plane can be determined by shaft axis and condyle axis. The coronal plane is parallel to the condyle axis and passes through the shaft axis. The sagittal plane can be obtained by shaft axis and coronal plane. The sagittal plane is perpendicular to the coronal plane and passes through the shaft axis (see in Fig.14).

D. AXIS-POSITION ALIGNMENT-BASED ITERATIVE REASSEMBLY

In this paper, we adopt the idea of iteratively conducting axis-position alignment to solve the assembling problem of fracture pieces. The pseudo code of the overall algorithm is given in Table 1. During the entire process of alignment, the femur shaft pieces is fixed and we only adjust the femur head pieces. In each iteration, the alignment is carried out in a coarse-to-fine strategy, the details are as follows.

1) COARSE ALIGNMENT

a: AXIS ALIGNEMNT

The neck-shaft angle and femoral anteversion angle are measured and adjusted to fall into the normal ranges.

TABLE 1. Pseudo code of our algorithm.

Algorithm 1: Axis-position alignment method

Data: Two fracture piece M_1 and M_2, iteration number N and convergency threshold δ.

Result: Transform matrix (R, t)

begin

Extract the semantic regions of M_1 and M_2 by including head region (S_1), neck region (S_2), shaft region (S_3), condyles region (S_4) and fracture surfaces (F_1, F_2) in Section III.C.(1);
M_1 is identified as the femoral head pieces according to S_1;
M_2 is identified as the femoral shaft pieces according to S_3;
Calculate the landmarks including head center (C_1), neck center (C_2), condyle centers (C_3, C_4);
Obtain the three axes in Section III.C.(2):
l_{hn} denotes head-neck axis by connecting C_1 and C_2;
l_c denotes condyle axis by connecting C_3 and C_4;
l_s denotes shaft axis by fitting a line to region S_3;
Calculate the datum planes including axial plane (P_1), coronal plane (P_2) and sagittal plane (P_3) in Section III.C.(3);
Initialize translation matrix (R) and rotation matrix (t) to zero;
k=0;
$M_1^0 = M_1$
While *Iteration* $k < N$ **do**
Calculate neck-shaft angle (α) and anteversion angle (β):
α is calculated by using l_{hn}, l_s and P_2;
β is calculated by using l_{hn}, l_c and P_1;
if *angles* α *and* β *are normal* **then**
Translate the M_1 along three axes.
Calculate Euclidean distance between F_1 and F_2;
Calculate translation matrix $t^{(k)}$;
else
Update α and β to the normal range;
Calculate rotation matrix $R^{(k)}$;
end
Refine $(R^{(k)}, t^{(k)})$ using the ICP;
$M_1^{(k)} = R^{(k)} M_1^0 + t^{(k)}$
If $(k > 0$ and $\left\| M_1^{(k)} - M_1^{(k-1)} \right\| < \delta)$
break;
$k = k + 1$;
end
end

The neck-shaft angle is adjusted by rotating around y-axis and the femoral anteversion angle is adjusted by revolving around z-axis.

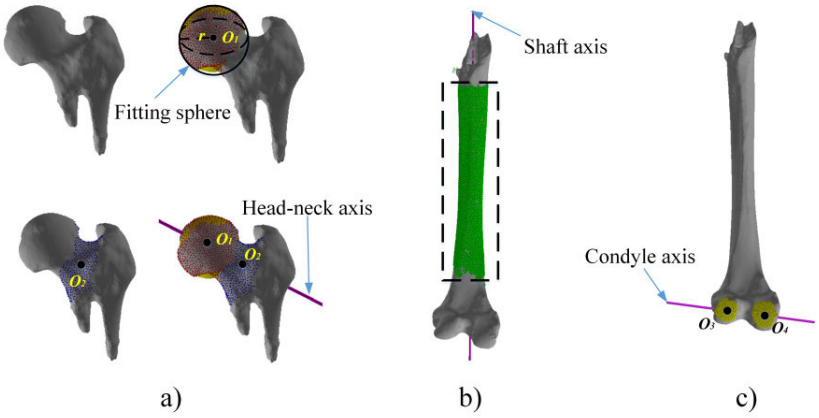

FIGURE 13. The details of axes' extraction. a) The head neck axis. b) The shaft axis. c) The condyle axis.

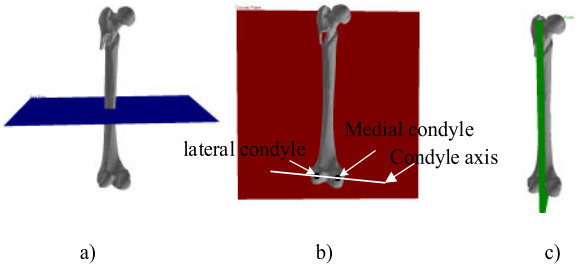

FIGURE 14. The datum planes. a) Axial plane, b) Coronal plane, and c) Sagittal plane.

b: POSITION ALIGNEMNT

To reduce the influence of noisy data, based on the axis alignment, 10% of the point pairs with the largest Euclidean distance between the fracture surfaces of two main bone pieces are removed. After that, the distance between the corresponding points of the fracture surfaces is calculated (See Equation (1)). And then the position of the femoral head piece is gradually adjusted by respectively translating along the x-axis, y-axis and z-axis until the minimum Euclidean distance value is found, and the corresponding transformation matrix is simultaneously recorded.

2) REFINE ALIGNMENT

a: REDUCTION CORRECTION

The Iterative Closest Point (ICP) method is used to refine the reduction results.

IV. RESULT

A. DATASETS

We collect clinical human bone data from the department of orthopaedics at Liyang People's Hospital, Changzhou, China. The data comprise 8 fracture femur models and 40 healthy femur models, represented as the 3D triangular mesh models, manually reconstructed from the clinical Computed Tomography (CT) images by using the software Mimics. All the trabecular bones are manually removed from the fracture bones. Parameters of the CT scanner are as follows: tube voltage 120 kV, tube current 200 mA, slice thickness 1 mm, layer pitch 0.5 mm, matrix 512×512.

The authors have received approval from Chinese Clinical Trial Registry (ID: ChiCTR1900023259), and to the best of their knowledge, certify that the patients undergoing treatment have given their informed consent to the collection and use of data for research purposes. This project is conducted with full respect to the privacy rights of all human subjects involved.

B. DATA PRE-PROCESSING

All the 3D bone models' trabecular bones are manually removed in the pre-processing procedure. Specifically, only the femoral head piece and the femoral shaft piece are preserved for each fracture model. The healthy models are leveraged to generate the training data for the deep neural network (see the details in Appendix).

C. EVALUATIONS & RESULTS

The evaluations are conducted in four aspects, i.e., evaluation of semantic regions, comparison with the clinical medical reduction standard, comparison with manual alignment and comparison with baseline methods.

1) EVALUATION OF SEMANTIC REGIONS

Extracting semantic regions is the key step in our approach. To evaluate the accuracy of extracting regions (anatomical regions and fracture surfaces), we compared the regions extracted by our method with the regions manually labeled by orthopaedic surgeons. The region manually labeled by surgeons is taken as ground-truth. We visually illustrate the difference between the manual extraction and the one by our method, as shown in Fig.15. Besides, we use the accuracy and recall of all semantic regions for evaluation. Accuracy (A) is simply a ratio of correctly predicted observation to the total observations (see in Equation (5)), and recall (R) is the ratio of correctly predicted positive observations to the all observations (see in Equation (6)).

$$A = \frac{TP + TN}{P + N} \tag{5}$$

$$R = \frac{TP}{TP + FN} \tag{6}$$

where TP denotes the number of correct extracted points in the semantic regions, TN denotes the number of correct extracted points in non-semantic regions, P denotes the number of ground-truth points in semantic regions, N denotes the number of ground-truth points in non-semantic regions, and FN denotes the number of wrong points extracted in semantic regions.

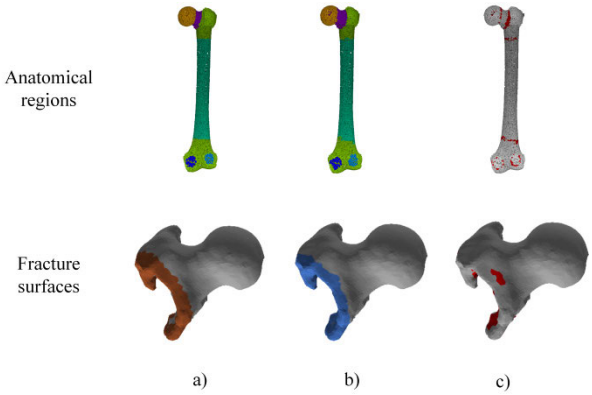

FIGURE 15. Visualized evaluation of semantic regions extraction. Top row: the visualized evaluation of anatomical regions. Bottom row: visualized evaluation of fracture surface. a) The result of surgeons' manual marks. b) The extracted results by our method. c) The errors between two results are highlighted in red.

The results of the extracted semantic regions of all the clinical cases are shown in Fig.16. As can be seen in Table 2, the accuracy of all regions is above 85% and the recall rate is above 87%. The results are similar to those of manual labeling by surgeons.

FIGURE 16. Experimental results of axis and position alignment-based reduction. First column: the source data. Second column: the semantic regions extracted by network. Third column: the fracture surface (blue). Forth column: manual reduction results. Fifth column: pairwise reduction with our method. End column: comparison between the distance errors with two methods. (Blue regions reflect low error, and red regions reflect high error).

2) COMPARISON WITH THE CLINICAL MEDICAL REDUCTION STANDARD

In clinical evaluation, the quality of the intertrochanteric fracture reduction will be usually evaluated according to the fracture angulation and the distance between fracture pieces. The clinical evaluation for bone reduction, w.r.t. axis alignment and position alignment, can be divided into three categories: good reduction, acceptable reduction, and poor reduction [1], as shown in Table 3.

The experimental results are shown in Fig. 16 as well as in Table 4, where the neck-shaft angle is between 125° and 145°, the anteversion angle is less than 20°, and the distance between bone fragments is less than 4 mm. All of the reduction results can be evaluated as good according to

TABLE 2. Anatomical regions evaluations.

Regions		Accuracy	Recall
anatomical regions	Head	92.3%	98.1%
	Neck	95.7%	93.8%
	Shaft	93.2%	94.9%
	Condyle	95.4%	93.2%
Fracture surface		85.7%	87.1%

the clinical criteria (see Table 3). In conclusion, all of the experimental results meet the axis and position alignment criteria of clinical reduction, with clinical practical value.

3) COMPARISON WITH THE MANUAL ALIGNMENT

The results of our method are compared with the results of manual reduction which are taken as the ground truth. The manual reduction results were performed by five orthopaedic surgeons, and the best one was taken as the final ground truth.

The reduction accuracy is evaluated by utilizing three metrics, i.e., the distance between bone fragments, translational error, and rotational error. The comparison is shown in Table 4, where MSE denotes the sum of the squared Euclidean distances between the corresponding points of the two fragments, α denotes the rotational error around the x-axis, β denotes the rotational error around the y-axis, and θ denotes the rotational error around the z-axis. Judging from the averaged distance errors and rotational errors, we can see that the results of our method exhibit low differences from the ground truth.

The error of the average distance between bone fragments is 1.0 ± 0.5 mm, the rotational error around the x-axis is $5 \pm 3°$, the rotational error around the y-axis is $5 \pm 5°$, and the rotational error around the z-axis is $5 \pm 4°$. According to Table 4, the results of our method exhibit, which are acceptable by the orthopaedic surgeons.

4) COMPARISON WITH BASELINE METHODS

Our method is compared with ICP algorithm [32] as well as the method proposed by the work of Paulano et al [33]. For the former baseline, the extracted fracture surfaces are aligned by ICP algorithm. For the latter baseline, we extract the fracture zone as shown in Fig.17. We decide to use distance filter to extract the final fracture zone because of its good performance on our data set. The reduction results of Paulano et al are obtained based on the fracture zone.

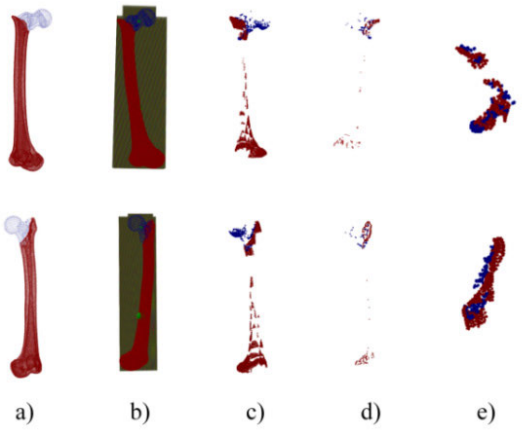

FIGURE 17. The details of extracting fracture zone by [33] a) The point clouds of models. b) The grid structure of each pieces. c) Extraction of the candidate points. d) Extraction of the fracture zone using curvature filter. e) Extraction of the fracture zone using distance filter.

We compare the two baselines with our method by three metrics, namely, displacement, angles and overlapping. The displacement denotes the distance between fracture zones of two major bone pieces. The angles include the anteversion angle and the neck-shaft angle. The overlapping error is defined as the ratio between overlapping voxels and touching voxels [33]. When bone fragments are moved or rotated with respect to their original position, the Paulano et al's method requires a previous rough alignment to make bone pieces have a good initial position. In order to compare the reduction results in more detail, for the Paulano et al's method, we calculated the reduction results with and without rough alignment, respectively.

The comparison is visualized in Fig.18 and is shown in Table 5 and Table 6. The details of results are analyzed as follows.

a: DISPLACEMENT EVALUATION

The displacements of results are less than 4 mm for all methods, which is in accordance with the standard of clinical reduction (See Table 3).

b: ANGLES EVALUATION

The neck-shaft angle and anteversion angle calculated by ICP and Paulano et al's method (without rough alignment)

TABLE 3. Clinical criteria for reduction of intertrochanteric fractures.

Evaluation criteria	Details	Reduction results
(1) Axis alignment	a) Neck-shaft angle greater than 125° and less than 145° b) Femoral anteversion angle less than 20°	a) Good: (1) and (2) met b) Acceptable: (1) or (2) met c) Poor: neither (1) nor (2) met
(2) Position alignment	The distance between bone fragments should be no more than 4 mm	

TABLE 4. Detailed experimental results.

Experiment	Mesh size (points)	Our method			Ground truth		MSE	Rotational error (degree)
		Neck-shaft /anteversion angle (degree)	Displacement (mm)	Runtime (min)	Neck-shaft /anteversion angle (degree)	Displacement (mm)		
1	219884	137.325/15.852	2.552	61	140.340/16.731	2.680	13.147	$\alpha = 5.92$ $\beta = 0.51$ $\theta = 1.06$
2	170967	126.117/14.331	2.236	42	129.354/13.572	1.788	21.198	$\alpha = 7.91$ $\beta = 1.2$ $\theta = 9.61$
3	164848	132.861/11.985	2.283	32	128.121/14.357	1.637	26.152	$\alpha = 6.07$ $\beta = 9.42$ $\theta = 8.83$
4	173521	129.567/13.542	2.127	45	128.460/15.325	1.063	30.088	$\alpha = 5.73$ $\beta = 11.88$ $\theta = 9.44$
5	179571	127.489/12.476	1.856	33	125.119/14.651	1.238	12.869	$\alpha = 5.03$ $\beta = 6.63$ $\theta = 1.27$
6	165191	125.764/15.367	1.479	37	129.355/15.268	1.309	46.234	$\alpha = 7.89$ $\beta = 1.96$ $\theta = 6.77$
7	186212	125.981/17.584	2.930	46	129.475/16.358	1.507	38.860	$\alpha = 3.42$ $\beta = 9.04$ $\theta = 9.84$
8	205684	133.441/15.865	2.457	55	135.125/13.227	1.608	44.350	$\alpha = 2.25$ $\beta = 3.44$ $\theta = 4.36$

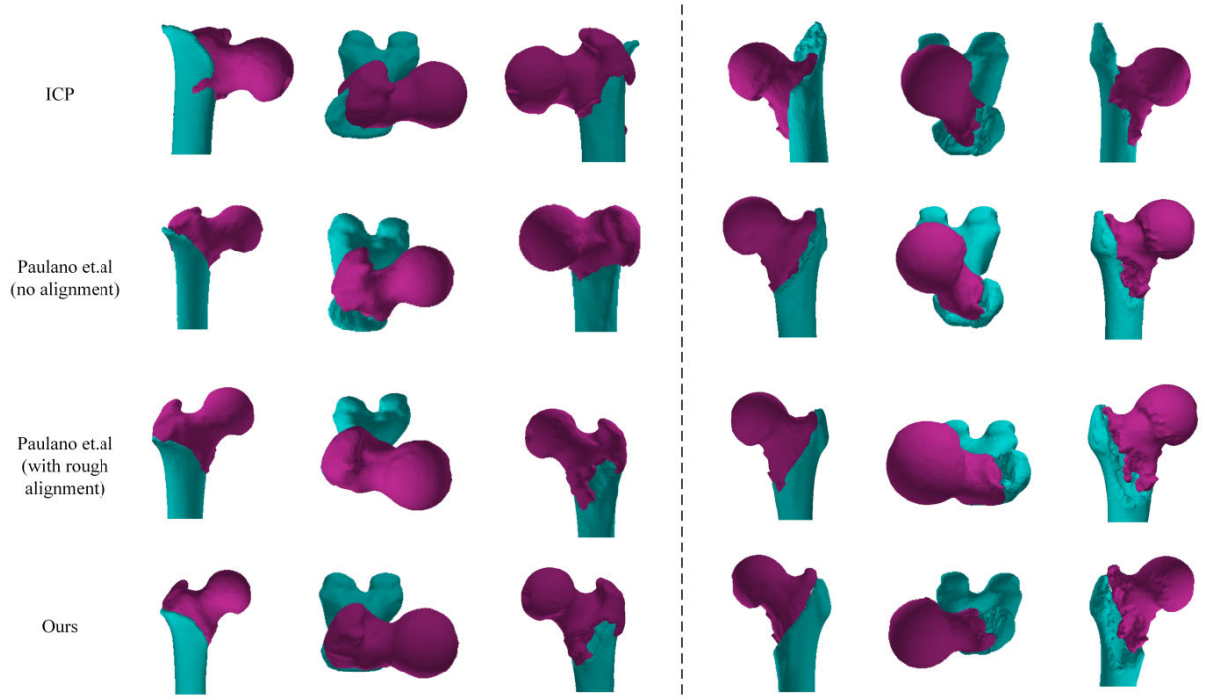

FIGURE 18. Comparison between our method and other methods. (Top) ICP algorithm. (Second row) Paulano et.al without rough alignment. (Third row) Paulano et.al with rough alignment. (Bottom) Our approach.

method are not up to the clinical medical reduction standard of intertrochanteric fracture (See Table 3). On the contrary, the two angles of Paulano et al (with rough alignment) and ours stay in the normal range of the standard. Such results justify the importance of axis alignment.

c: OVERLAPPING EVALUATION

The obtained mean overlapping error of our method and Paulano et al's method (rough alignment) is very small. But the errors of ICP algorithm and Paulano et al's method without rough alignment are higher than those of our

TABLE 5. Qualitative evaluations.

	Neck-shaft /anteversion angle(degree)			Displacement (mm)
	Min	Max	mean	mean
ICP	88.52/ -30.45	144.71/ 45.23	97.23/ -10.43	2.79
Paulano (without rough alignment)	94.23/ -14.39	135.64/ 20.71	110.65/ -5.33	1.95
Paulano (with rough alignment)	122.34/ 10.45	139.53/ 14.58	125.82/ 12.37	**1.91**
Ours	125.98/ 11.98	137.32/ 17.58	129.30/ 14.44	2.11

TABLE 6. Overlapping and touching evaluations.

	Touching cells (mean)	Overlapping cells (mean)	Overlapping/Touching ratio (Overlapping error)
ICP	2312	524	0.2266
Paulano (without rough alignment)	1910	317	0.1659
Paulano (with rough alignment)	1108	98	0.0884
Ours	981	82	**0.0835**

method as well as Paulano et al's method with rough alignment.

Our method is implemented on the Microsoft Visual Studio 2015 platform. The experiment took 32 to 61 minutes, as shown in Table 3. The running time of the method was related to the number of points in the bone piece model. Our method is much more efficient than the manual method.

V. DISSCUSSION

This paper proposes a data-driven method to extract the bone axes and iteratively solve the constrained assembly problem for the intertrochanteric fractures. In clinics, assembling intertrochanteric fractures considers only two primary bone pieces, i.e., the femoral piece and the femoral shaft piece. Thus, our goal is to assemble these two pieces to assure the axes angles to be in the normal range, and the fracture boundaries should be as close as possible.

The main advantages of our method are as follows. First, the proposed method is more suitable for clinical reduction allowing for both axis-alignment and position alignment. Second, the semantic regions of fracture pieces are automatically extracted by using a neural network.

In the following, some issues will be discussed in detail.

The first issue is about the extraction of fracture surfaces. The reasons of why the method of [9] can be leveraged to extract the fracture surfaces are two-folds. On one hand, the trabecular bones are removed from the input fracture bone models in the pre-processing step. Then, the left bones' fracture surfaces will be extracted more precisely without the disturbance of the inner soft tissues. On the other hand, we further refine the fracture surface by merging the fracture surfaces and trimming out the outliers on the semantic regions.

The second issue relates to the extraction of semantic regions. In most of the cases, the global morphology of the fracture bone is still approximate to that of the healthy bone. As a result, the semantic regions of the fracture bones can be precisely extracted by deep learning, if the healthy bones are used as training data for the deep neural network. The tests conducted demonstrated that the semantic regions extraction of each case performs good in our dataset. Note that in the settings of the severe comminuted fractures, the semantic regions will be probably damaged, causing inaccurate semantic extraction and reduction failures. In practice, the comminuted fractures account for low percentage of the bone fractures.

The third issue to be discussed lies in the user-input parameters of our method. Our method relies on user-defined values which hinders our method from the fully-automatic approach. The user-defined thresholds, including the normal threshold of fracture surface extraction and the distance threshold of fracture surface post-processing, have to be adjusted in order to adapt our method to the available data.

One limitation is that our method is not resilient to the lower resolution of triangle mesh models. Besides, our methods will also fail in the scenarios when the scanned fractured femurs lack the distal segments.

VI. CONCLUSION

We present a data-driven method to meet the two requirements of axis-position alignment assembling for intertrochanteric fractures. The key idea of this method is to pair-wisely assembling the bone pieces through iterative axis alignment and position alignment. We utilize a neural network to robustly compute the pieces' semantic regions, since extracting these regions is a non-trivial problem due to the randomness of the fracture. Besides, our assembling method ensures both the positional and axial alignment to meet the clinical requirements of the intertrochanteric fractures. The experimental results show that our method is capable of meeting the criteria of good clinical reduction. In addition, the assembly results by our method are proved to be closed to those of manual alignment by surgeons and outperforming the two typical assembling methods.

Our future effort can be focused on how to address more challenging problems such as assembling complex bones with bone dislocation and bone deformation.

ETHICAL APPROVAL

Ethics clearance was obtained from the institutional Ethics Committee at The People's Hospital of Liyang. We can confirm that Chinese Clinical Trial Registry Approval was given (ID: ChiCTR1900023259). The patients undergoing treatment gave their informed consent to the collection and use of data for research purposes. The privacy rights of human subjects always be observed.

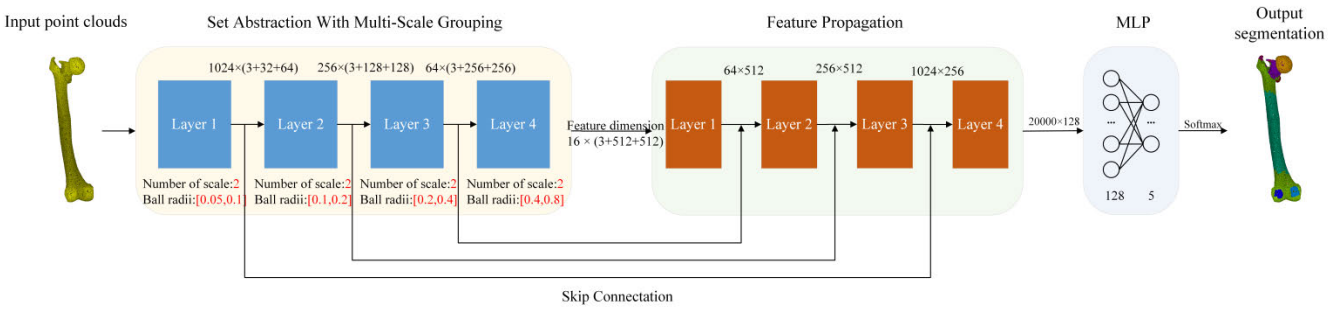

FIGURE 19. Architecture of the semantics extraction network, which is implemented based on PointNet^{++}. The network takes a 3D point cloud of size 20000 as input, and outputs final segmentation result.

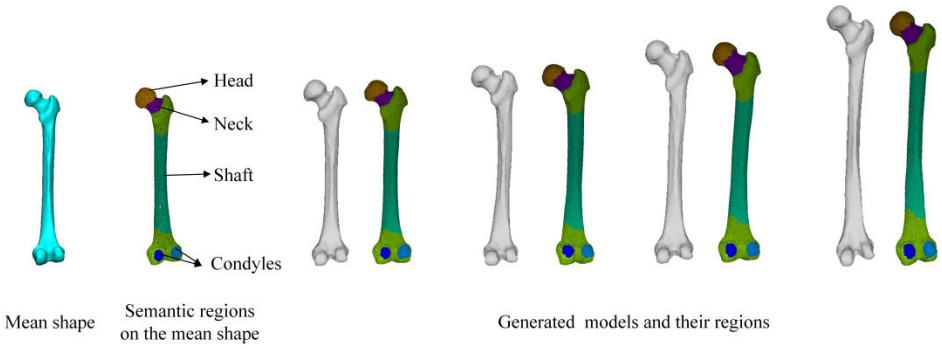

FIGURE 20. The synthetic models created by statistical shape model and semantic regions on template and synthetic models.

APPENDIX

A. NETWORK ARCHITECTURE AND NETWORK TRAINING

1) NETWORK ARCHITECTURE

A neural network is trained to identify the medical semantics of bone fractures. The network is implemented based on PointNet^{++}, as illustrated in Fig.19. The pipeline includes three stages as follows. The first stage (four set abstraction layers) down-samples the input point cloud extracts local patterns. Specifically, the first stage includes four layers. The second stage (four feature propagation layers) up-samples the point cloud to its original size and propagate features by interpolating feature values. The third stage (two fully-connected layers) further refines the features. Softmax function is appended to the end of the fully-connected layers. Both input and output of the network are normalized by the min-max scalar to [0, 1]. To keep the number of the input point set fixed, the network uniformly samples 20000 points among the set of the vertices of the input mesh.

2) NETWORK TRAINING DATA

The training set contains 300 synthetic femur models, which are created by randomly deforming the statistical shape model [30]. As illustrated in Fig.20, we build the statistical shape model [30] of the healthy femur bone. The statistical shape model of the femur bone is constructed by using 40 healthy femur mesh models. Based on these data, we perform Principal Component Analysis (PCA) [34] to obtain the statistical femoral model, which contains the mean shape, top 30 principal vectors and corresponding principal values. As stated in [30], a statistical shape model can be formulated as follows.

$$\boldsymbol{S}(x) = \boldsymbol{S}_{mean} + \sum_{l=1}^{L} \boldsymbol{\alpha} \boldsymbol{u}_l \tag{7}$$

where $\boldsymbol{S}_{mean}$ denotes the mean shape of the 40 healthy femur models, $\boldsymbol{a} = (\boldsymbol{a}_1, \boldsymbol{a}_2, \cdots, \boldsymbol{a}_l)$ denotes the coefficient vector, $\boldsymbol{u}_l$ denotes the principal vectors with the corresponding principle values of top L values, $L = 30$. In this paper, the training data, we call generated models thereinafter, are generated by randomly sampling the coefficient $\boldsymbol{a}$.

The generated model and the mean shape have the same topology. Thus, the semantic regions can be obtained by label propagation. Specifically, we can label the mean shape $\boldsymbol{S}_{mean}$ and map the label of the mean model's vertex to the generated model's vertex with the same vertex ID. Surgeons are invited to label the semantic regions of the mean shape (see Fig.20).

3) NETWORK TRAINING

We use the Adam optimizer with a learning rate of 0.01, and train the network for 200 epochs with a batch size of 20. We randomly select 20% of the training data as the

validation set, and perform dataset augmentation by random scaling, rotation, translation, and perturbation. On a single NVIDIA RTX 6000 graphics card, network training takes around four hours.

REFERENCES

[1] N. K. Kanakaris, T. H. Tosounidis, and P. V. Giannoudis, "Nailing intertrochanteric hip fractures: Short versus long; locked versus non-locked," *J. Orthopaedic Trauma*, vol. 29, pp. S10–S16, Apr. 2015, doi: 10.1097/BOT.0000000000000286.

[2] D. Hernandez, R. Garimella, A. E. M. Eltorai, and A. H. Daniels, "Computer-assisted orthopaedic surgery," *Orthopaedic Surg.*, vol. 9, no. 2, pp. 152–158, May 2017, doi: 10.1111/os.12323.

[3] J. J. Jiménez-Delgado, F. Paulano-Godino, R. PulidoRam-Ramírez, and J. R. Jiménez-Pérez, "Computer assisted preoperative planning of bone fracture reduction: Simulation techniques and new trends," *Med. Image Anal.*, vol. 30, pp. 30–45, May 2016, doi: 10.1016/j.media.2015.12.005.

[4] I. Pountos and P. V. Giannoudis, "The management of intertrochanteric hip fractures," *Orthopaedics Trauma*, vol. 30, no. 2, pp. 103–108, Apr. 2016, doi: 10.1016/j.mporth.2016.03.004.

[5] H. Wolfson, E. Schonberg, A. Kalvin, and Y. Lamdan, "Solving jigsaw puzzles by computer," *Ann. Operations Res.*, vol. 12, no. 1, pp. 51–64, Dec. 1988, doi: 10.1007/BF02186360.

[6] Q.-X. Huang, S. Flöry, N. Gelfand, M. Hofer, and H. Pottmann, "Reassembling fractured objects by geometric matching," *ACM Trans. Graph.*, vol. 25, no. 3, pp. 569–578, Jul. 2006, doi: 10.1145/1141911.1141925.

[7] T. Okada, Y. Iwasaki, T. Koyama, N. Sugano, Y.-W. Chen, K. Yonenobu, and Y. Sato, "Computer-assisted preoperative planning for reduction of proximal femoral fracture using 3-D-CT data," *IEEE Trans. Biomed. Eng.*, vol. 56, no. 3, pp. 749–759, Mar. 2009, doi: 10.1109/TBME.2008.2005970.

[8] W. Yu, M. Li, and X. Li, "Fragmented skull modeling using heat kernels," *Graph. Models*, vol. 74, pp. 140–151, Jul. 2012, doi: 10.1016/j.gmod.2012.03.011.

[9] P. Fürnstahl, G. Székely, C. Gerber, J. Hodler, J. G. Snedeker, and M. Harders, "Computer assisted reconstruction of complex proximal humerus fractures for preoperative planning," *Med. Image Anal.*, vol. 16, no. 3, pp. 704–720, Apr. 2012, doi: 10.1016/j.media.2010.07.012.

[10] L. Hu, J. Zhang, C. Li, Y. Wang, Y. Yang, P. Tang, L. Fang, L. Zhang, H. Du, and L. Wang, "A femur fracture reduction method based on anatomy of the contralateral side," *Comput. Biol. Med.*, vol. 43, no. 7, pp. 840–846, Aug. 2013, doi: 10.1016/j.compbiomed.2013.04.009.

[11] J. Buschbaum, R. Fremd, T. Pohlemann, and A. Kristen, "Computer-assisted fracture reduction: A new approach for repositioning femoral fractures and planning reduction paths," *Int. J. Comput. Assist. Radiol. Surgery*, vol. 10, no. 2, pp. 149–159, Feb. 2015, doi: 10.1007/s11548-014-1011-2.

[12] E. Tsamoura and I. Pitas, "Automatic color based reassembly of fragmented images and paintings," *IEEE Trans. Image Process.*, vol. 19, no. 3, pp. 680–690, Mar. 2010, doi: 10.1109/TIP.2009.2035840.

[13] K. Zhang and X. Li, "A graph-based optimization algorithm for fragmented image reassembly," *Graph. Models*, vol. 76, no. 5, pp. 484–495, Sep. 2014, doi: 10.1016/j.gmod.2014.03.001.

[14] M. M. Bronstein, J. Bruna, Y. LeCun, A. Szlam, and P. Vandergheynst, "Geometric deep learning: Going beyond Euclidean data," *IEEE Signal Process. Mag.*, vol. 34, no. 4, pp. 18–42, Jul. 2017, doi: 10.1109/MSP.2017.2693418.

[15] E. Altantsetseg, K. Masuyama, and K. Konno, "Pairwise matching of 3D fragments using fast Fourier transform," in *Vis. Comput.*, vol. 30, pp. 929–938, May 2014, doi: 10.1007/s00371-014-0959-9.

[16] L. Vlachopoulos, G. Székely, C. Gerber, and P. Fürnstahl, "A scale-space curvature matching algorithm for the reconstruction of complex proximal humeral fractures," *Med. Image Anal.*, vol. 43, pp. 142–156, Jan. 2018, doi: 10.1016/j.media.2017.10.006.

[17] S. Winkelbach and F. M. Wahl, "Pairwise matching of 3D fragments using cluster trees," *Int. J. Comput. Vis.*, vol. 78, no. 1, pp. 1–13, Jun. 2008, doi: 10.1007/s11263-007-0121-5.

[18] G. Papaioannou and E. A. Karabassi, "On the automatic assemblage of arbitrary broken solid artefacts," *Image Vis. Comput.*, vol. 21, pp. 401–412, May 2003, doi: 10.1016/s0262-8856(03)00008-8.

[19] K. Subburaj, B. Ravi, and M. Agarwal, "Computer-aided methods for assessing lower limb deformities in orthopaedic surgery planning," *Computerized Med. Imag. Graph.*, vol. 34, no. 4, pp. 277–288, Jun. 2010, doi: 10.1016/j.compmedimag.2009.11.003.

[20] K. Subburaj, B. Ravi, and M. Agarwal, "Automated identification of anatomical landmarks on 3D bone models reconstructed from CT scan images," *Computerized Med. Imag. Graph.*, vol. 33, no. 5, pp. 359–368, Jul. 2009, doi: 10.1016/j.compmedimag.2009.03.001.

[21] P. Cerveri, A. Manzotti, N. Confalonieri, and G. Baroni, "Automating the design of resection guides specific to patient anatomy in knee replacement surgery by enhanced 3D curvature and surface modeling of distal femur shape models," *Computerized Med. Imag. Graph.*, vol. 38, no. 8, pp. 664–674, Dec. 2014, doi: 10.1016/j.compmedimag.2014.09.001.

[22] B.-K. Park, J.-H. Bae, B.-Y. Koo, and J. J. Kim, "Function-based morphing methodology for parameterizing patient-specific models of human proximal femurs," *Comput.-Aided Des.*, vol. 51, pp. 31–38, Jun. 2014, doi: 10.1016/j.cad.2014.02.003.

[23] B. Liu, S. Hua, H. Zhang, Z. Liu, X. Zhao, B. Zhang, and Z. Yue, "A personalized ellipsoid modeling method and matching error analysis for the artificial femoral head design," *Comput.-Aided Des.*, vol. 56, pp. 88–103, Nov. 2014, doi: 10.1016/j.cad.2014.06.009.

[24] B. Liu, W. Liu, S. Zhang, M. Wang, Y. Yang, X. Zhang, W. Qi, and X. Qu, "An automatic personalized internal fixation plate modeling framework for minimally invasive long bone fracture surgery based on pre-registration with maximum common subgraph strategy," *Comput.-Aided Des.*, vol. 107, pp. 1–11, Feb. 2019, doi: 10.1016/j.cad.2018.08.004.

[25] S.-Y. Baek, J.-H. Wang, I. Song, K. Lee, J. Lee, and S. Koo, "Automated bone landmarks prediction on the femur using anatomical deformation technique," *Comput.-Aided Des.*, vol. 45, no. 2, pp. 505–510, Feb. 2013, doi: 10.1016/j.cad.2012.10.033.

[26] H. Jacinto, S. Valette, and R. Prost, "Multi-atlas automatic positioning of anatomical landmarks," *J. Vis. Commun. Image Represent.*, vol. 50, pp. 167–177, Jan. 2018, doi: 10.1016/j.jvcir.2017.11.015.

[27] C. R. Qi, L. Yi, H. Su, and L. J. Guibas, "PointNet++: Deep hierarchical feature learning on point sets in a metric space," in *Proc. Adv. Neural Inf. Process. Syst.*, 2017, pp. 5099–5108.

[28] R. Hanocka, A. Hertz, N. Fish, R. Giryes, S. Fleishman, and D. Cohen-Or, "MeshCNN," *ACM Trans. Graph.*, vol. 38, no. 4, pp. 1–12, Jul. 2019, doi: 10.1145/3306346.3322959.

[29] Z. Wu, S. Song, A. Khosla, F. Yu, L. Zhang, X. Tang, and J. Xiao, "3D ShapeNets: A deep representation for volumetric shapes," in *Proc. IEEE Conf. Comput. Vis. Pattern Recognit. (CVPR)*, Jun. 2015, pp. 1912–1920, doi: 10.1109/CVPR.2015.7298801.

[30] T. F. Cootes, C. J. Taylor, D. H. Cooper, and J. Graham, "Active shape models-their training and application," *Comput. Vis. Image Understand.*, vol. 61, no. 1, pp. 38–59, Jan. 1995, doi: 10.1006/cviu.1995.1004.

[31] H. Späth, "Least-square fitting with spheres," *J. Optim. Theory Appl.*, vol. 96, no. 1, pp. 191–199, Jan. 1998, doi: 10.1023/A:1022675403441.

[32] P. J. Besl and N. D. McKay, "A method for registration of 3-D shapes," *IEEE Trans. Pattern Anal. Mach. Intell.*, vol. 14, no. 2, pp. 239–256, Feb. 1992, doi: 10.1109/34.121791.

[33] F. Paulano-Godino and J. J. Jiménez-Delgado, "Identification of fracture zones and its application in automatic bone fracture reduction," *Comput. Methods Programs Biomed.*, vol. 141, pp. 93–104, Apr. 2017, doi: 10.1016/j.cmpb.2016.12.014.

[34] S. Wold, K. Esbensen, and P. Geladi, "Principal component analysis," *Chemom. Intell. Lab. Syst.*, vol. 2, pp. 37–52, Aug. 1987, doi: 10.1016/0169-7439(87)80084-9.

ZIYUE DENG was born in Henan, China, in 1993. He received the B.E. degree in computer science from Hohai University, Changzhou, China, in 2016, where he is currently pursuing the Ph.D. degree. His current research interests include computer graphics and deep geometric learning.

JUNFENG JIANG was born in Jiangsu, China, in 1979. He received the Ph.D. degree in computer science from Hohai University, China, in 2013. He is currently an Associate Professor with Hohai University. His research interests include computer-aided pre-operative planning for orthopaedics, computer graphics, and deep geometric learning.

HONGWEI LIU was born in Jiangsu, China, in 1973. He received the M.D. degree in clinical medicine from Soochow University, China, in 2015. He is currently a chief physician of orthopaedics in The Second People's Hospital of Changzhou. His research interests include digital orthopaedics and 3D printing technology in medicine.

ZHENGMING CHENG received the Ph.D. degree from Zhejiang University, China, in 2001. He was a Visiting Scientist with the City University of Hong Kong, in 2003. He is currently a Professor and the Director of the Department of Computer Science, College of Internet of Things (IOT) Engineering. His current research interests include feature modeling and recognition, CAD/CAM integration, computer graphics, and virtual reality. He is a senior member of CCF and a member of CCF TCCADCG.

RUI HUANG received the B.S. degree in aircraft manufacturing engineering and the M.S. degree in aeronautics and astronautics manufacturing engineering from Northwestern Polytechnical University, China, in 2009 and 2010, respectively, and the Ph.D. degree from the School of Mechanical Engineering, Northwestern Polytechnical University, China, in 2016. He is currently an Assistant Professor with the College of IOT Engineering, Hohai University, China. His research interests include CAD/CAM, 3D CAD model retrieval, and computer graphics.

WENXI ZHANG was born in Jiangsu, China, in 1971. He graduated in clinical medicine from Nanjing Medical University, China, in 1995. He is currently a chief physician of orthopaedics in The People's Hospital of Liyang. His research interests include digital orthopaedics and medical device research and development.

KUNJIN HE received the master's and Ph.D. degrees from the College of Computer Science and Information Engineering, Hohai University. He was a Visiting Scholar with the ECE Department, University of New Mexico, USA, in 2016. He is currently a Professor with the College of IOT Engineering, Hohai University. His main research interests include orthopedic implants digital technology, CAD, and geometric modeling.